Tellus (1982), *34*, 567–578

Assessment of the separate effects of baroclinicity and thermal stability in the atmospheric boundary layer over the sea

By SYLVAIN M. JOFFRE, *Institute of Marine Research, PL 166, SF-00141 Helsinki 14, Finland*

(Manuscript received September 15, 1981; in final form February 1, 1982)

ABSTRACT

Pibal soundings taken during the period 1929 to 1936 were analysed to augment our knowledge of boundary layer climatology. Use of the geostrophic departure method enables computation of surface stress and the cross-isobar angle as functions of stability and baroclinicity, the latter being assessed from the upper wind shear. The comparative effects of both terms are discussed and the importance of the often-neglected baroclinicity in explaining the scatter of the computed parameters is stressed. Use of similarity theory enables us to achieve some further order in the data and eventually to estimate the universal functions A and B freed from baroclinic effects.

1. Introduction

Our understanding of the physics of the atmospheric boundary layer (ABL) has made great progress during the last 15 years. We are, however, hampered by the lack of climatological data on the whole ABL, which would help us to relate the synoptical structure to boundary layer scale phenomena when making, say, local forecasts. Moreover, when such climatological studies are undertaken, they generally involve gross statistics that include all influencing parameters. As a result, it is difficult to distinguish between the intrinsic effects of each influencing parameter. Furthermore, the effect on the ABL of large-scale disturbances, such as the little-studied horizontal temperature inhomogeneities, deserves more attention. Similarity theories have been favoured during the last decade, and we shall apply them here to extract additional information not revealed by climatological statistics. This paper is an attempt to contribute to the study of these aspects through analysis of old pibal soundings carried out over the Baltic Sea. The research was initiated by the need to parametrize large-scale stress over a frozen sea; hence only winter-time data are considered.

2. The data and analysis

A series of pilot balloon soundings suitable for the present study was performed between June 1929 and June 1936 on Utö (cf. Fig. 1), an island lying about 80 km southwest of mainland Finland ($\varphi = 59°47'$ N, $\lambda = 21°22'$ E). The location of this island on the southern margin of the Åland Archipelago favours investigations on the marine ABL. The data consist of optically performed pilot sounding measurements giving wind velocity V and wind direction α averaged over intervals of 100 m up to 1 km and of 500 m above that height. Surface wind velocity V_s and direction α_s are reported for a height of $z_a = 15$ m. The only profiles considered here are those reaching at least 500 m; thus, all average profiles contain the same number of composite profiles up to 500 m. For the sake of comparison, both ice-free and ice-covered periods are analysed for February and March of the years in question. A total of 250 profiles was available, including 57 profiles for sea-ice situations. The majority of the soundings (63%) were performed at 0900L. Air temperature T_a ($z_t = 2$ m) was available from the Utö station, and sea surface temperature T_w (average ~0.5 °C) was measured about every

 0040-2826/82/060567-12$02.50/0

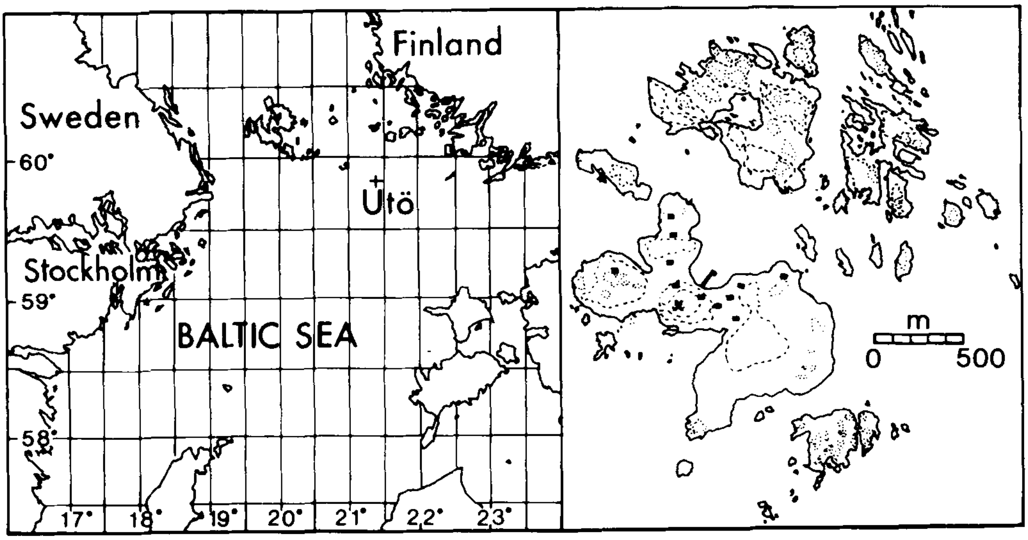

Fig. 1. The study area; in the insert a topographical map of Utö island showing the location of the observation site (×) and the 5 m height contours (dashed lines).

2 weeks when the sea was open about 1 km west of Utö. Note that the proximity of the mainland implies a strong temperature gradient at the sea surface during mild winters. The small size of the island, the lack of vegetation and the ever-present wind in this period of negligible radiative effect make the value of T_a a fair indicator of the marine surface layer air temperature. On the other hand, the air-sea temperature difference was much stronger in unstable cases (~ -3.6 °C) than in stable cases (~ 1.6 °C). Thus the error in T_a or T_w (~ 0.2 °C) may be of greater importance under the latter conditions.

The structure of the turbulent ABL depends largely on thermal stability, which is assessed through a bulk Richardson number defined as

$$\mathrm{Ri}_s = \frac{g}{T_a} \frac{(T_a - T_w)/z_t}{(V_s/z_a)^2}. \qquad (1)$$

This gives a stability parameter for open-sea situations only. On an ice-covered sea, the unknown ice surface temperature is highly dependent on solar radiation, air temperature and the physical and mechanical properties of the ice itself, thus making it impossible to assess Ri_s. Owing to the geographical configuration of the study area, one can expect the climatological structure of the boundary layer on Utö to be strongly related to the origin of the air masses sweeping over the island. This is supported by the clear correlation between the surface wind direction α_s and the stability parameter Ri_s (Joffre, 1978). The majority of stable cases exist in the range (120°–300°) and unstable cases in the range (300°–120°). This means that the stable runs correspond to winds blowing over the sea and the unstable runs to winds coming from cold mainland Finland. Frontal activity is common at these latitudes, and the discharge of cold northerly winds behind a cyclone results in unstable thermal conditions over the sea. Since large-scale features leave such a strong mark on the stability of the lowest levels of the atmosphere over the open sea, one can expect a similar distribution of stability according to wind direction when the sea is covered by ice (this will be shown in Section 5.1). Accordingly, the data were divided into 3 main groups: 124 open water situations with $\mathrm{Ri}_s \leqslant 0$ (index U), 69 open water situations with $\mathrm{Ri}_s > 0$ (index S) and 57 sea ice situations (index I). Further, each of these basic groups may be divided into 6 subgroups according to surface wind direction. Some subjectivity has been introduced in the choice of the range of these direction groups by using a homogeneous geographical origin and the correlation between α_s and Ri_s. These subgroups are:

(1) $0° \leqslant \alpha_s < 80°$ winds from mainland Finland (mainly very unstable);

(2) $80° \leqslant \alpha_s < 110°$ winds from the Gulf of Finland (mainly unstable);
(3) $110° \leqslant \alpha_s < 170°$ winds from Estonia (mainly neutral);
(4) $170° \leqslant \alpha_s < 240°$ winds from the Baltic Proper (mainly stable);
(5) $240° \leqslant \alpha_s < 290°$ winds from Sweden (mainly stable);
(6) $290° \leqslant \alpha_s < 360°$ winds from the Archipelago (mainly unstable).

3. Local climatology

3.1. *The wind rose*

The evolution of the wind rose with height might be expected to show a general clockwise rotation of the characteristic features of the data rose, but this is not apparent in the wind roses for 500 m and 1000 m (Joffre, 1978). Indeed, although the Southerlies, Southwesterlies and Westerlies turn clockwise, the Northeasterlies and Northerlies seem to rotate counter-clockwise. This means that a thermal wind effect compensates the frictional veering. Cold advection decreases the veering of the wind (this applies to the Northeasterlies and Northerlies) whereas warm advection increases the veering. Thus, a thermal wind from the Northwest sector is inferred, a conclusion that is supported by distribution maps of the average upper temperature (e.g. Guterman and Hanevskoi, 1963). As there is little difference between the roses at 500 m and 1000 m, the turning of the wind evidently occurs mainly in the first 500 metres of the atmosphere, which may be taken as a rough estimate of the mean height of the ABL.

3.2. *The velocity ratio*

A meteorologist wishing to make a local wind forecast from the geostrophic wind would be helped by a knowledge of statistics, e.g. of a velocity ratio defined as $R = V_s/V(500)$. Our overall mean of 0.75 agrees with the results of Hasse and Wagner (1971), who obtained values of the ratio $R = V(10)/V_g$ between 0.7 and 0.8 for the geostrophic wind velocity V_g within the range 10–20 m s^{-1}, which is close to the value of 0.8 obtained by Findlater et al. (1966) for the ratio $V(18)/V(900$ mb) at the Atlantic weather ships I (52° N 20° E) and J (59° N 19° E). As has been noted in all earlier studies, the ratio is generally higher for weak 500 m winds ($V(500) \lesssim 10$ m s^{-1}). The ratio R is obviously strongly dependent on stability, since wind shear is a function of stability. The overall mean for R increases from 0.68 under stable conditions to 0.77 under ice conditions and to 0.78 under unstable conditions. Roll (1965) quoted values for the ratio V_s/V_g from 0.55 to 0.8 when the air-sea temperature difference $(T_a - T_w)$ varies from +4 °C to −8 °C. The behaviour of R, according to surface wind direction reveals the same general trend for the three main groups of data with higher values in the range 80°–240° and lower values in the range 240°–80°. Since the latter range includes opposite conditions of stability (241°–290° and 291°–360°) and opposite conditions of surface roughness (241°–290° and 0°–80°), the trend observed is probably also due to baroclinicity.

3.3. *Wind veering*

Owing to the variable balance of forces in the boundary layer with upward-decreasing friction, wind direction is a function of height. We use the quantity $\Delta\alpha = \alpha(500) - \alpha_s$, which expresses the turning of the wind in the 0–500 m layer. The overall mean of 17° is somewhat higher than the values obtained by Findlater et al. (1966) at ships I and J (7° and 9°, respectively) and those reported by Mendenhall (1967) from Johnston Island (6°) and ship N (2°), though smaller than the latter's value from Swan Island (21°). Backing of the wind ($\Delta\alpha < 0$) at $z = 500$ m was observed in 6% of the stable cases and 31% of the unstable ones. These values are consistent with the observations by Sheppard et al. (1952) that in 30% of cases the wind at 300 m was backed on the surface wind (their median $T_a - T_w$ was −0.8 °C). As expected, the veering angle $\Delta\alpha$ in the lowest 500 m is greatest under stable conditions (31°) and lowest under unstable conditions (8°); an intermediate value of 17° was found for ice conditions. The wind shows a strong backing (−18°) for the group S1. This direction range corresponds to wind blowing from over cold mainland Finland. The implied cold advection will cause counter-clockwise rotation that can be as strong as 70° (Hoxit, 1974) and can easily explain the value we obtained.

4. Computation of baroclinic boundary layer characteristics

4.1. *Method*

Our goal is to study the separate dependence of boundary layer parameters such as surface stress and cross-isobaric angle on stability and baroclinicity. Relevant in this context is the ageostrophic method, in which baroclinicity is estimated from the geostrophic shear (rather constant according to our data). Its extrapolation to the surface gives the surface geostrophic wind. This method is applicable to stationary conditions, so we shall apply it to the mean profiles formed from the groups defined in Section 2. We use Lettau's method as described in Johnson (1962) to which we include baroclinicity explicitly. Integrating the steady state equation of motion from the surface to a level H_1 at which the stress vanishes yields

$$\tau_0 = \rho f \int_0^{H_1} (\bar{v} - V_g)\, dz \tag{2}$$

$$O = \rho f \int_0^{H_1} (\bar{u} - \bar{U}_g) dz \tag{3}$$

where ρ is the air density, f the Coriolis parameter, (u, v) and (U_g, V_g) the longitudinal and lateral components of the actual and geostrophic wind, respectively and τ_0 the surface stress. We have taken here the x-axis oriented along the surface shear. In the computation we take $H_1 = 2000$ m to allow geostrophic adjustment. As tested in a few cases, the smoothness of the upper profiles, however, makes the results insensitive to the choice of H_1. The second equation (3) will be a useful constraint for assessing the geostrophic wind profile.

The assumption of a constant geostrophic shear yields $U_g = U_{go} + S_u z$ and $V_g = V_{go} + S_v z$ where (U_{go}, V_{go}) are the surface geostrophic components and (S_u, S_v) the constant slopes of the components. Substituting these linear profiles into (3) and using the fact that $U_{gI} = U_g(z = H_I) = \bar{u}(H_I)$ yields

$$U_{go} = \frac{2}{H_I} \int_0^{H_I} \bar{u}\, dz - \bar{u}(H_I). \tag{4}$$

Since the $\bar{u}$ profile is known, U_{go} is fully determined by eq. (4). The lowest point of intersection of the linear geostrophic wind profile with the observed $\bar{u}$ profile determines a level Z^* at which the lateral stress τ_{yz} is at a maximum, since τ_{yz} increases up to this height and then decreases in the interval between Z^* and H_I. Integrating the equations of motion again, but now from the surface to this height Z^* yields

$$\tau_{xz}^* = \rho f \int_{Z^*}^{H_I} (\bar{v} - V_g)\, dz \tag{5}$$

$$\tau_{yz}^* = \rho f \int_0^{Z^*} (\bar{u} - U_g)\, dz, \tag{6}$$

where we have substituted the expression (2) for the surface stress into (5) and used $\tau_{ij}^* = \tau_{ij}\ (z = Z^*)$. Since both the $\bar{u}$ and U_g profiles are now known, the term τ_{yz}^* can be computed. On the other hand, the semi-empirical parametrization of the vertical stress components, with the identity of the eddy diffusivity coefficient K_m for both components, gives at the level $z = Z^*$

$$K_m^* = \tau_{xz}^* \Big/ \left(\rho \frac{\partial \bar{u}}{\partial z}\right)^* = \tau_{yz}^* \Big/ \left(\rho \frac{\partial \bar{v}}{\partial z}\right)^*. \tag{7}$$

The slopes of the $\bar{u}$ and $\bar{v}$ profiles at $z = Z^*$ can be determined graphically; τ_{xz}^* is then obtained from the right identity of eq. (7). Further, substituting (6) and (7) into (5) and using the property of constant geostrophic shear leads to the following expression for the lateral component of the geostrophic wind:

$$V_{go} = \frac{\displaystyle\int_{Z^*}^{H_1} \bar{v} dz - \frac{V_{gI}}{2H_1}(H_1^2 - Z^{*2}) - \left[\left(\frac{\partial \bar{u}}{\partial z}\right)^* \Big/ \left(\frac{\partial \bar{v}}{\partial z}\right)^*\right] \int_0^{Z^*} (\bar{u} - U_g)\, dz}{(H_1 - Z^*)\left(1 - \dfrac{H_1 + Z^*}{2H_1}\right)}. \tag{8}$$

Once V_{go} is known, the computation of the surface stress τ_0 from eq. (2) is straightforward. We are also able to compute the cross-isobar angle α_0 defined as

$$\alpha_0 = \tan^{-1}\left(\frac{V_{go}}{U_{go}}\right), \tag{9}$$

which expresses the deviation of the surface wind from the surface geostrophic wind. The simplest parametrization of the wind stress for modelling studies is through a drag coefficient C_d or geostrophic drag coefficient C_g in the expressions

$$\tau_0 = \rho C_d V_s^2, \tag{10}$$

$$\tau_o = \rho C_g G_0^2, \tag{11}$$

where $G_0^2 = U_{go}^2 + V_{go}^2$. These coefficients, which primarily represent the surface roughness, vary with the wind velocity itself and with thermal stability, and although abundant empirical data have been compiled for these variations, some disagreement still exists about the results. This may be because the field measurements are representative only of the actual place where they were carried out. Moreover it is difficult to compare conditions of inhomogeneity, unsteadiness and baroclinicity between one place and another. Further, the interpretation of C_g in the baroclinic case is not straightforward since it cannot be directly interpreted in terms of free-stream velocity. However, G_0 is the wind concept used in the resistance laws (cf. eqs. (13)) and has the desired properties in the asymptotic case of barotropy.

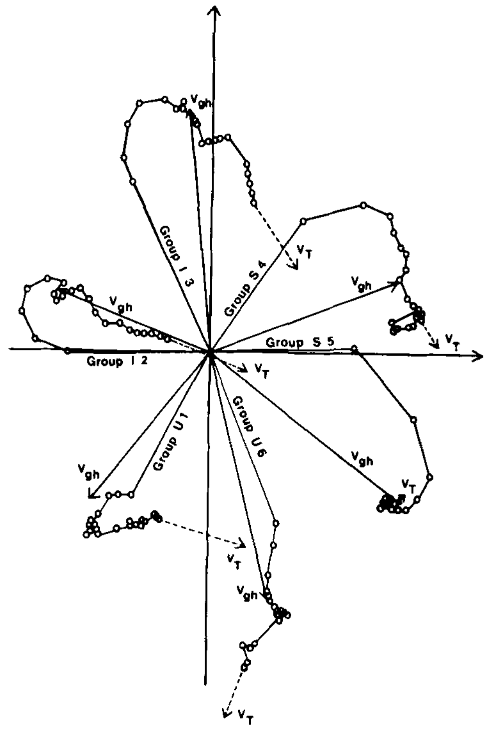

Fig. 2. Typical hodographs for some of the mean profiles: groups U1, U6, I2, I3, S4 and S5. $\mathbb{V}_T$ is the thermal wind vector for the layer $(0–H_1)$, $\mathbb{V}_{gh}$ the geostrophic wind at $z = h$. The first point of a hodograph represents surface wind, the next ones the wind vector extremity at $z = k \cdot 100$ m with $k = 1, 2, 3, \ldots$.

4.2. *Results for the surface drag*

The computational procedure described in the previous section was applied to 14 selected mean profiles differentiated by stability and surface wind direction. The hodographs of some of these profiles with the computed thermal wind vector are shown in Fig. 2. The geostrophic wind vector at the top of the ABL is also represented in these hodographs. The computed geostrophic wind and the observed wind profiles were in close agreement above 1000 m (cf. Table 3), and thus supported the assumptions made. The results of the computation are given in Table 1. In a few cases, a decrease in the number of available data led to a marked kink at a given level H_c of the upper profile. The integration was then performed only up to this height H_c in order to maintain the smoothness of the profiles. The cross-isobar angle values α_0 show the expected decreasing trend from large values under stable conditions (mean 27°) to smaller values (mean 16.5°) under unstable conditions. The drag coefficients and surface stress values show a large scatter. On one occasion (group I4), the surface stress even has a negative value. However, the implied momentum transfer from the sea surface towards the atmosphere is unlikely owing to the much higher wind than ice velocity; this group will be deleted from forthcoming analyses. The very high value of C_d or τ_0 found for the group U1 originates from the computation of the $\bar{u}$ profile slope at $z = Z^*$ (cf. eq. 7), which was very small here, thus making τ_{xz}^* very uncertain. This is because the eddy viscosity concept of eq. (7) becomes inapplicable under strongly unstable conditions, since vertical gradients vanish. However, it

Table 1. *Parameters computed with the ageostrophic method for the different mean groups. N is the number of profiles included in the mean, G_0 (ms^{-1}) the surface geostrophic wind velocity, α_0 the cross-isobar angle, $\Delta\alpha$ (500) the wind veering angle at 500 m, C_d the drag coefficient, C_g the geostrophic drag coefficient, τ_0($10 \times$ N m^{-2}) the surface stress, Ri_s the mean surface Richardson number and H_c (in metres) the upper height of integration, if not 2000 m*

	Open water stable cases			Ice covered						Open water unstable cases				
	S4	S5	S6	I1	I2	I3	I4	I5	I6	U1	U3	U4	U5	U6
N	26	24	15	11	4	6	9	10	16	43	9	11	16	38
G_0	9.4	11.5	9.4	8.2	10.2	13.6	10.4	9.4	10.8	12.1	12.2	9.2	9.6	10.6
α_0	27.6°	37.0°	17.0°	16.0°	21.9°	15.1°	18.5°	30.0°	22.4°	33.7°	19.3°	12.5°	14.3°	2·3°
$\Delta\alpha$ (500)	33.0°	40.6°	17.7°	12.0°	27.7°	18.5°	17.5°	30.8°	9.8°	4.2°	6.3°	17.6°	11.1°	7.7°
$C_d \times 10^3$	0.49	1.59	0.92	0.36	1.82	1.64	—	0.81	3.18	10.27	4.94	0.93	3.12	1.08
$C_g \times 10^3$	0.33	0.57	0.51	0.31	0.79	0.69	—	0.47	1.36	4.18	3.26	0.66	1.75	0.74
τ_0	0.35	0.90	0.54	0.24	1.00	1.55	−0.04	0.50	1.92	7.34	5.86	0.68	1.92	1.00
$\overline{\mathrm{Ri}}_s$	0.20	0.20	0.09	—	—	—	—	—	—	−0.85	−0.30	−0.48	−0.10	−0.43
H_c		1500		1800				1900						

is also evident from the hodograph (cf. Fig. 2) that this profile was profoundly disturbed and far from the conventional Ekman spiral and corresponded to the strongest mean temperature gradient (Northeasterlies). Note that the magnitude of deformation of the hodographs from theoretical Ekman spirals is proportional to the strength of the thermal wind and that the axis of deformation corresponds well to the thermal wind direction.

Averaging the values of C_d and C_g over all the direction groups, we find the representative mean values shown in Table 2. These values fall in the expected range of magnitude as reported by Garratt (1977) for C_d over open water. For C_g our values agree well with Deacon's (1973) finding of 0.73×10^{-3} at sea and Brocks and Krügermeyer's (1972) observed value of 0.6×10^{-3}. Using the ageostrophic method for a near-neutral situation, Lettau (1957) and Lettau and Hoeber (1964) obtained a smaller value, 0.48×10^{-3}, for the Scilly and Helgoland pibal profiles. Our value of C_d for unstable conditions seems to be too high. However, this value is influenced by the very large value of the group U1 discussed above; without it we would get $C_d \approx 2 \times 10^{-3}$.

Table 2. *Average values of surface and geostrophic drag coefficients*

	$C_d \times 10^3$	$C_g \times 10^3$	$\overline{\mathrm{Ri}}_s$	N
Stable	1.00 ± 0.45	0.47 ± 0.10	0.162	65
Ice	1.56 ± 0.97	0.72 ± 0.36	—	47
Unstable	4.07 ± 3.43	2.12 ± 1.39	−0.432	117

The drag coefficient C_d depends primarily on surface characteristics, i.e. it is a local parameter, but, like the state of the sea, these characteristics themselves are non-local phenomena. This contradiction is probably one of the main reasons for the great variation of C_d found in the literature. Hence, it seems natural to introduce the geostrophic drag coefficient relating surface drag to large-scale forcing velocity. Further, the standard deviation for C_g is less than for C_d although C_g involves more processes than C_d. Fewer data are available for the drag of sea ice, and a summary of them is found in Banke et al. (1976). Sea-ice always presents irregularities due to the pressure forces driving ice-floes against each other. These "larger-scale" features may be taken into account when assessing the wind drag through the introduction of a form drag concept. The values reported, however, fall in the same range as those for open-sea situations.

Finally, one must keep in mind that the use of average profiles in our computations will lead to larger values of the drag coefficients, since second-order quantities are not linear with respect to the operation of averaging (i.e. $\overline{V^2} \geqslant \bar{V}^2$).

4.3. *Intrinsic effect of baroclinicity*

Using the assumption of constant geostrophic shear, we computed in Section 4.1 the components of geostrophic shear (S_u, S_v), where S_u is the projection on an x-axis aligned with the surface wind and S_v is its normal component in a direct rotation of the axis. We also computed the angle β_0 between the surface geostrophic wind and the thermal wind. The values for each direction and stability group are given in Table 3. With the axis chosen, a warm advection occurs when the angle β_0 is approximately in the range (0°, 180°) with the maximum effect around $\beta_0 = 90°$, whereas cold advection occurs for β_0 in the range (180°–360°).

The dependence of the cross-isobar angle α_0 on β_0 is shown in Fig. 3. The interpretation of this curve is not straightforward since there are only 14 scattered empirical points. Nonetheless, it is possible to distinguish a sine-like trend with smaller values of α_0 for warm air advection cases ($\beta_0 \approx$ 0°–180°) and larger values for cold air advection cases, the amplitude being about 15°. The points corresponding to strong stable cases (shown by an arrow in the figure) have very large values of α_0 and thus depart clearly from the other points. Thus, stable stratification would impose its large cross-isobar angle by providing strong resistance to the baroclinic effect. Stable stratification seems to present an effective barrier to the expected downward transport of additional momentum originating from the geostrophic shear which would normally oppose the flow towards lower pressure, i.e. reduce the cross-isobar angle of the surface wind (Hoxit, 1974). This effect can be compared to

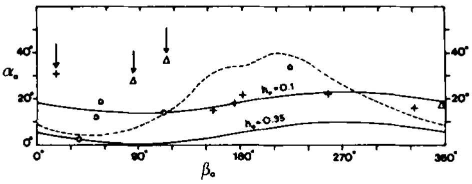

Fig. 3. Variation of the cross-isobar angle α_0 with the angle between the thermal wind and the surface geostrophic wind. The triangles are for stable conditions, the crosses for ice situations, and the open circles for unstable conditions. The arrows point to the very stable mean runs. The dashed curve represents the corresponding observations by Hoxit (1974) and the continuous lines the theoretical model of Arya (1975) for two different values of the parameter $h_* = hf/u_*$.

the zero-wind shear profiles in the convective well-mixed boundary layer, although baroclinicity is present with a marked geostrophic shear as was shown by Arya and Wyngaard (1975).

For comparison, the curve corresponding to the analysis of nearly 23,000 radiosoundings by Hoxit (1974) and the curve from a model of Arya (1975) are drawn in the same figure (Fig. 3). In his model, Arya uses the parameters $h_* = hf/u_*$ (where h is the actual height of the ABL) and $\hat{u} = \langle V \rangle / u_*$ ($\langle V \rangle$ is a mean mixed layer velocity), whereas for the thermal wind magnitude he uses $M_0 = hS_0/u_*$ (with $S_0^2 = S_u^2 + S_v^2$). For our data, the mean value of M_0 turns around 5, $\hat{u} \approx 30$ with $\langle V \rangle$ approximately estimated by the quantity $h^{-1}{}_0\int^h \bar{V}\,dz$ and our h_* ranges mainly between 0.1 and 0.35. The curves corresponding to the latter two enveloping values, which are represented in Fig. 3, appear

Table 3. *Characteristic parameters of the baroclinic ABL for the different mean groups. S_u and S_v (in s^{-1}) are the two components of the geostrophic shear, β_0 is the angle between the surface geostrophic wind and thermal wind measured clockwise from the latter, h is the actual height (in metres) of the ABL determined from the mean profiles, $\zeta_h = h/L_*$ is the stability parameter and $h_* = hf/u_*$. $(\partial\bar{u}/\partial z)_f$ and $(\partial\bar{v}/\partial z)_f$ are the observed mean wind shears in the layer 1–2 km*

	Open water stable cases			Ice covered						Open water unstable cases				
	S4	S5	S6	I1	I2	I3	I4	I5	I6	U1	U3	U4	U5	U6
$S_u \times 10^3$	−0.61	−0.51	0.81	3.22	−3.73	−3.85	−2.85	1.57	0.25	−0.97	0.52	0.69	−1.54	1.98
$S_v \times 10^3$	−1.46	−0.28	−0.20	0.64	1.56	−0.60	0.65	−1.61	1.64	4.19	−2.06	−1.44	−2.10	−1.67
β_0	85°	114°	357°	333°	181°	156°	175°	16°	257°	223°	57°	52°	112°	38°
h	700	700	400	400	600	600	700	500	500	1000	600	600	800	700
ζ_h	30.9	31.3	7.3	—	—	—	—	—	—	−91.6	−24.5	−35.2	−13.6	−38.0
h_*	0.52	0.32	0.24	0.35	0.26	0.21	—	0.25	0.16	0.16	0.11	0.32	0.25	0.30
$(\partial\bar{u}/\partial z)_f$	−0.34	−0.50	1.07	3.21	−4.13	−4.63	−4.25	1.84	−0.52	−2.08	0.69	1.89	−1.94	1.55
$(\partial\bar{v}/\partial z)_f$	−0.34	−0.27	−0.56	0.54	2.38	−0.81	1.94	−0.93	1.56	2.10	−3.51	−1.54	−2.05	−2.75

to explain most of our data. The only points remaining outside are the strongly stable cases discussed above and two very unstable cases. The location of both points can be explained by the fact that their $\hat{u}$ value is definitively lower than that for other profiles; according to Arya's model, this implies an overall upward shift of the curves. According to Arya and Wyngaard (1975), Hoxit's curve corresponds to $M_0 = 19$, which explains its larger amplitude. A higher-order model by Arya and Wyngaard (1975) and observational data analysed by Bernstein (1973) give the same qualitative agreement. The variation of $\Delta\alpha$ as a function of β_0 indicates the opposite trend to $\alpha_0(\beta_0)$. In fact, its maximum occurs during warm air advection and its minimum during cold air advection. This is also in accordance with Hoxit's (1974) findings.

As has been pointed out by Sheppard et al. (1952), the effect of baroclinicity is not limited to its action on wind veering; it also changes the vertical shear of the horizontal wind in the boundary layer, which in turn modifies the turbulent transport of momentum and the stress profiles. A measurement of the drag is the ratio V_s/G_0, which is shown in Fig. 4. The scatter of the observation points is conspicuously small, and even differentiation according to thermal stability does not appear clearly. For comparison, the corresponding curve by Hoxit is plotted in the same figure, but with an overall upward shift of 0.23 from its mean value of 0.51 to our mean value of 0.74 in order to compensate for the rougher case of Hoxit. The two curves are rather similar except for a delayed phase lag of our empirical data with respect to those of Hoxit. This is related to the phase shift δ in the expression for the baroclinic universal functions A and B (Arya, 1978), where δ is essentially dependent on stability. This would imply that, on the average, Hoxit's data correspond to more stable conditions than do ours, i.e. they

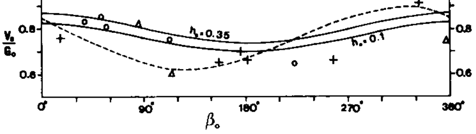

Fig. 4. Dependence of the ratio V_s/G_0 on the thermal wind direction with respect to surface isobars. For explation see caption to Fig. 3.

have larger δ values. The same mixed layer model results obtained by Arya (1975) are also shown in this figure for $h_* = 0.1, 0.35$ (still with $\hat{u} = 30$ and $M_0 = 5$). Note that our data are in phase with the theoretical model curves. The maximum now occurs close to $\beta_0 = 0$. In other words, the additional downward momentum transfer induced by the geostrophic shear results, for a given geostrophic wind, in an increase in the surface wind speed and a slight decrease in the cross-isobar angle (cf. Fig. 3). This study also gives some support to the simple and attractive vertically integrated model proposed by Arya (1975).

5. The resistance laws

5.1. *Dimensionless profiles*

The behaviour of the wind profile in the ABL is very variable and depends on many external parameters. Hence, it is a cumbersome task to estimate the relative importance of each of these factors and their quantitative effect on the vertical structure of the wind. Nonetheless, some kind of order can be achieved by using similarity theories. According to general similarity theory, any parameter made properly dimensionless is a function of the following non-dimensional parameters (e.g. Arya, 1977)

$$z/h, \quad \zeta_h = h/L_*, \quad h_* = hf/u_*,$$

$$M_x = hS_u/u_*, \quad M_y = hS_v/u_*,$$

where $L_* = -u_*^3/(g\beta\kappa Q_0)$ is the Monin-Obukhov length scale (Q_0 being the kinematic heat flux) and $M_x = M_0 \cos\beta_0$, $M_y = M_0 \sin\beta_0$. Thus, it appears that the actual height of the ABL is a primary parameter for any investigation. This height h is rather easily determined from temperature profiles, but since we have no information on the thermal structure of the ABL, we shall assess it subjectively from wind profiles. The height h is taken as the level at which a jump or a sudden adjustment to the upper smoother profile occurs in unstable cases and as the top of the layer of significant shear in stable cases. If S_u and S_v are known, the geostrophic wind components U_{gh} and V_{gh} at this height can be determined. The vector $\mathbb{V}_{gh}$ is shown in the hodographs in Fig. 2. The values of h, ζ_h and h_*, are listed in Table 3. Determination of ζ_h requires knowledge of L_*, which, in open sea situations, is determined from Ri_s using the relations given by Pruitt et al. (1973).

Single wind profiles vary considerably. However, in the framework of the velocity defect laws

$$\frac{U_{gh} - \bar{u}(z)}{u_*} = F_u(z/h, \zeta_h, h_*, M_x, M_y),$$

$$\frac{V_{gh} - \bar{v}(z)}{u_*} = F_v(z/h, \zeta_h, h_*, M_x, M_y), \tag{12}$$

where F_u and F_v are unknown dimensionless functions, profiles with similar values for the internal parameters will collapse into similar profiles along z/h. This is illustrated in Fig. 5 where the dependence on ζ_h explains much of the variability. Under stable conditions, the profiles show a strong overshooting for the longitudinal component, whereas unstable cases show a rather vertically homogeneous profile, especially for the lateral component. This enables us to characterize the stability group of the ice profiles, and it appears that this classification is consistent with the classification for the open-sea situations.

5.2. *Assessment of the universal functions A and B*

The velocity defect laws (12) apply to the outer layer of the ABL. Close to the surface, in the inner layer, one can derive the law of the wall. Reconciliating both laws by assuming a matching layer, one obtains the resistance laws which give the drag coefficients and the cross-isobar angle that depend on the two dimensionless universal functions A_i and B_i:

$$\kappa \frac{U_{g0}}{u_*} = \ln \frac{h}{z_0} - A_i(\zeta_h, h_*, M_x, M_y),$$

$$\kappa \frac{V_{g0}}{u_*} = -B_i(\zeta_h, h_*, M_x, M_y), \tag{13}$$

where κ is the Karman constant and z_0 the roughness length. Owing to the obvious advantage of having such universal predictive laws, much work has been devoted to assessing these universal functions from either empirical data or theoretical models. For open-water situations, we can determine z_0 from Charnock's (1955) relation $z_0 = mu_*^2/g$, where g is the acceleration due to gravity and m a constant that we take as equal to 0.0144 as in the review by Garratt (1977). The determination of A_i and B_i is then straightforward. However, functions depending upon 4 different parameters are rather intractable. Fortunately, Arya and Wyngaard (1975) managed to give an expression for A_i and B_i from some simple arguments related to the equality of mass flow in barotropic and baroclinic conditions. The interesting outcome of this theory is that the functions can be decomposed into their barotropic and baroclinic components, i.e.:

$$A_i(\zeta_h, h_*, M_x, M_y) = A_{bp}(\zeta_h, h_*) + \tfrac{1}{2}\kappa M_0 \cos(\beta_0 - \delta),$$

$$B_i(\zeta_h, h_*, M_x, M_y) = B_{bp}(\zeta_h, h_*) + \tfrac{1}{2}\kappa M_0 \sin(\beta_0 - \delta), \tag{14}$$

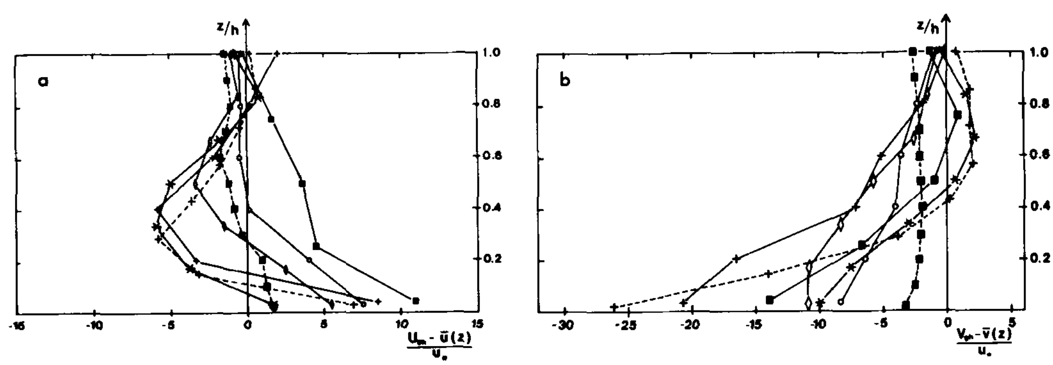

Fig. 5. Dimensionless longitudinal (a) and lateral (b) velocity-defect profiles for all ice groups, one typical water stable run (S5) and one typical water unstable run (U1). Full squares (■): subgroup 1; asterisks (*): subgroup 2; diamonds (◇): subgroup 3; triangles (△): subgroup 4; crosses (+): subgroup 5; open circles (○): subgroup 6.

where δ is a phase angle depending essentially on ζ_h (Arya, 1978) and the index bp refers to the barotropic mode. Thus, the functions A_i and B_i may be computed from eqs. (13). Substitution of their values in (14) permits the calculation of A_{bp} and B_{bp} with the baroclinic effects eliminated. These last values of A and B show a slightly smaller scatter. The results are given in Table 4, and the dependence of A_{bp} and B_{bp} on stability is illustrated in Fig. 6.

Arya (1977) summarized the latest results of universal function determination and proposed some semi-empirical relationships for A and B; in unstable cases they read:

$$A_{bp} = \ln(-\zeta_h) + \ln h_* + 1.5, \quad \zeta_h \leqslant -2,$$
$$B_{bp} = \kappa h_*^{-1} + 1.8\, h_* \exp(0.2\zeta_h); \tag{15}$$

and in stable cases

$$A_{bp} = -\frac{0.96}{a}\zeta_h + \ln \zeta_h + 2.5 - \ln a, \quad \zeta_h \geqslant 2,$$

$$B_{bp} = \frac{1.15}{a}\zeta_h + 1.1, \tag{16}$$

where the coefficient a comes from the numerical factor scaling the stable boundary layer height to the quantity $(u_* L_*/f)^{1/2}$. Arya took $a = 1$ but, according to his figure 6, which showed the observed stable ABL heights, a value of 3.5 will be used here, as it fits better his intermediate and strong stability points. Note that the scatter is rather small for the angle function B but much larger for the function A. For adiabatic conditions, an eye fit gives $A(0) \approx 2$ and $B(0) \approx 4$, which is in close agreement with results found elsewhere.

Table 4. *Results of the computation for the universal similarity functions with and without baroclinic effects. A_i, B_i are determined by eqs. (13), and A_{bp}, B_{bp} by eqs. (14) using empirical δ-values from Arya (1978)*

	A_i	A_{bp}	B_i	B_{bp}	δ
S4	−2.90	−1.80	10.20	10.89	35°
S5	2.26	2.56	10.11	10.08	35°
S6	−1.34	−1.57	5.18	5.40	30°
U1	8.77	8.79	3.43	2.33	12°
U3	7.05	7.08	2.31	2.68	18°
U4	0.70	0.57	3.35	4.15	17°
U5	5.74	6.60	2.37	2.95	20°
U6	0.89	0.19	0.59	1.63	16°

6. Conclusion

It has been shown here that pibal soundings can contribute to our knowledge of the ABL

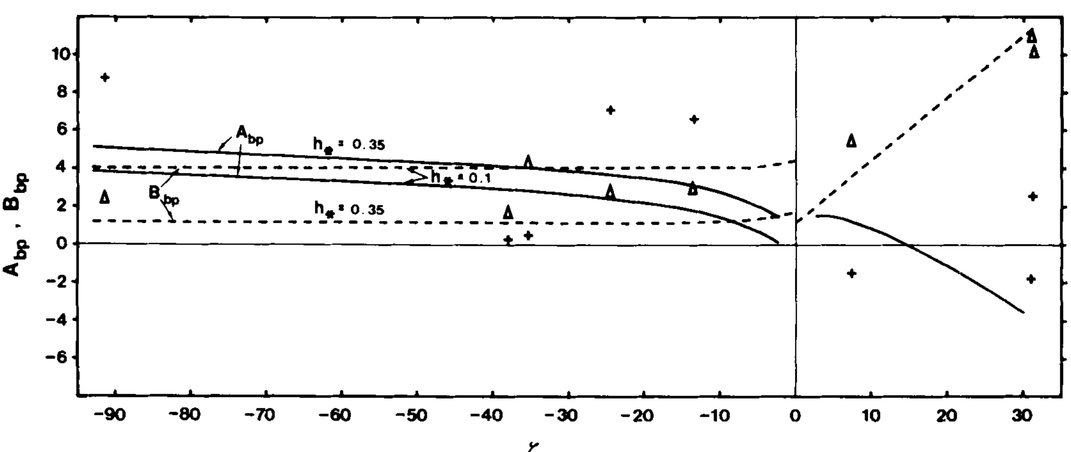

Fig. 6. Variations in the similarity functions A_{bp} (crosses) and B_{bp} (triangles) freed from baroclinic effects as a function of stability (ζ_h). The curves are from Arya's (1977) semi-empirical formulae (15) and (16) for A (continuous line) and B (dashed line).

climatology. The ageostrophic method is also shown to be applicable under certain conditions (stationarity, homogeneity of the data). The results stress the individual importance of stability and baroclinicity effects in ABL dynamics. The cross-isobar angle increases with stability and cold air advection and decreases with instability and warm air advection. The surface drag increases with instability, and parallelism of the thermal wind with the geostrophic wind. From this study it appears that, for very unstable or very stable conditions, buoyancy overwhelms baroclinic effects either by vigorous stirring or strong stratification. We also showed the advantage of using the framework of similarity theories for classifying the wind profiles in the ABL. Finally, the dependence of the universal functions A and B for the resistance laws on stability gives very reasonable results considering the large scatter generally encountered in studies of this kind, even in those with more accurate observation data.

This study shows the need for more observations of this kind. In the analysis of the data, however, a distinction should be made between the effects of thermal stability, roughness, baroclinicity, etc., whose relative effects are otherwise hidden in overall statistics.

7. Acknowledgements

I gratefully acknowledge the advice and support of Prof. E. Holopainen, Prof. S. A. Kitaigorodskii and Dr P. Mälkki. I also thank Dr J. Riissanen, who provided the basic data, and Mr S. Pietikäinen, who helped me with the data analysis. This research was supported by the Board of Navigation.

REFERENCES

Arya, S. P. S. 1975. Comments on "The influence of geostrophic shear on the cross-isobar angle of the surface wind". *Bound. Layer Meteorol. 8*, 239–242.

Arya, S. P. S. 1977. Suggested revisions to certain boundary layer parametrization schemes used in atmospheric circulation models. *Mon. Weather Rev. 105*, 215–227.

Arya, S. P. S. 1978. Comparative effects of stability, baroclinity and the scale-height ratio on drag laws for the atmospheric boundary layer. *J. Atmos. Sci. 35*, 40–46.

Arya, S. P. S. and Wyngaard, J. C. 1975. Effect of baroclinicity on wind profiles and the geostrophic drag law for the convective planetary boundary layer. *J. Atmos. Sci. 32*, 767–778.

Banke, E. G., Smith, S. D. and Anderson, R. J. 1976. Recent measurements of wind stress on Arctic sea ice. *J. Fish. Res. Board Can. 33*, 2307–2317.

Bernstein, A. B. 1973. Some observations of the influence of geostrophic shear on the cross-isobar angle of the surface wind. *Bound. Layer Meteorol. 3*, 381–384.

Brocks, K. and Krügermeyer, L. 1972. The hydrodynamic roughness of the sea surface. In *Studies in Physical Oceanography 1* (ed. A. Gordon). New York: Gordon and Breach, 75–92.

Charnock, H. 1955. Wind stress on a water surface. *Quart. J. Roy. Meteorol. Soc. 81*, 639–642.

Deacon, E. L. 1973. Geostrophic drag coefficients. *Bound. Layer Meteorol. 5*, 321–340.

Findlater, J., Harrower, T. N. S., Howkins, G. A. and Wright, H. L. 1966. Surface and 900 mb wind relationships. *Meteorol. Office Scientific Paper*, London *23*, 1–41.

Garratt, J. R. 1977. Review of drag coefficients over oceans and continents. *Mon. Weather Rev. 105*, 915–929.

Guterman, I. G. and Hanevskoi, I. V. 1963. *Aeroclimatological Atlas of the Northern Hemisphere* (in Russian). Hydrometeorological Publishing House, Leningrad.

Hasse, L. and Wagner, V. 1971. On the relationship between the geostrophic and surface wind at sea. *Mon. Weather Rev. 99*, 255–260.

Hoxit, L. R. 1974. Planetary boundary layer winds in baroclinic conditions. *J. Atmos. Sci. 31*, 1003–1020.

Joffre, S. M. 1978. Studies of the winter-time boundary layer over the Baltic Sea based on pilot balloon soundings. *Merentutkimuslaitoksen Julk. 243*, Helsinki, 3–62.

Johnson, W. B. Jr 1962. Climatology of atmospheric boundary layer parameters and energy dissipation, derived from Gregg's aerological survey of the U.S. In *Studies of the three-dimensional structure of the planetary boundary layer*, Final Report, Univ. of Wisconsin, Dept. of Meteor. 125–158.

Lettau, H. H. 1957. Windprofil, innere Reibung und Energieumsatz in den unteren 500 m über dem Meer. *Beitr. Phys. Atmos. 30*, 78–96.

Lettau, H. H. and Hoeber, H. 1964. Über die Bestimmung der Höhenverteilung von Schubspannung und Austausch-koeffizient in der atmosphärischen Reibungsschicht. *Beitr. Phys. Atmos. 37*, 105–118.

Mendenhall, B. R. 1967. A statistical study of frictional wind veering in the planetary boundary layer. *Atmos. Sci. Paper 116*, Dept. Atmos. Sci., Colorado State Univ., Fort Collins, 1–57.

Pruitt, W. O., Morgan, D. L. and Lourence, F. J. 1973.

Momentum and mass transfer in the surface boundary layer. *Quart. J. Roy. Meteorol. Soc. 99*, 370–386.
Roll, H. U. 1965. *Physics of the marine atmosphere.* In Van Mieghem (ed.), International Geophysics Series. New York. 426 pp.
Sheppard, P. A., Charnock, H. and Francis, J. R. D. 1952. Observations of the westerlies over the sea. *Quart. J. Roy. Meteorol. Soc.* **78**, 563–582.